Analysis of High-Speed Aerodynamics of a Swept Wing with Seamless Flaps (Invited)

Trong T. Bui[1]
NASA Armstrong Flight Research Center, Edwards, California 93523

Computational fluid dynamics (CFD) analysis was conducted to evaluate the high-speed aerodynamics of a Gulfstream GIII airplane (Gulfstream Aerospace Corporation, Savannah, Georgia) swept wing modified with an experimental seamless, compliant flap called the Adaptive Compliant Trailing Edge (ACTE) flap for airworthiness. The high-speed aerodynamics of the modified ACTE wing were analyzed at a Mach number of 0.85 and an altitude of 40,000 ft. A polyhedral finite-volume unstructured Reynolds-averaged Navier-Stokes CFD code was used with a two-equation turbulence model. Wing aerodynamics sensitivities to lift coefficients, airplane engine operation, vortex generators (VGs), and ACTE flap deflections were examined. High-speed flow over the clean GIII wing without VGs was found to be complex with outboard shock and boundary-layer interactions causing flow separation over the upper wing surface upstream of the aileron, which could result in buffet and controllability problems at higher lift coefficient values. The VGs were found to improve the high-speed aerodynamics of the clean wing, as expected; however, ACTE flap deflections of as little as 1 to 2 deg were found to negate all of the aerodynamic benefits provided by the VGs at high speeds.

I. Nomenclature

ACTE	=	Adaptive Compliant Trailing Edge
c	=	airfoil chord
BL	=	wing buttline station (in inches)
C_D	=	aircraft drag coefficient
C_L	=	aircraft lift coefficient
C_l	=	aircraft rolling moment coefficient
C_m	=	aircraft pitching moment coefficient
C_p	=	pressure coefficient
C_Y	=	aircraft side force coefficient
CFD	=	computational fluid dynamics
MAC	=	mean aerodynamic chord
NASA	=	National Aeronautics and Space Administration
OML	=	outer mold line
VGs	=	vortex generators
x	=	streamwise distance
y^+	=	normal distance to the wall in boundary-layer wall units

II. Introduction

The National Aeronautics and Space Administration (NASA) Armstrong Flight Research Center (Edwards, California) (AFRC) SubsoniC Research Aircraft Testbed (SCRAT) tail number 804,[1] is a modified Gulfstream III (GIII) (Gulfstream Aerospace Corporation, Savannah, Georgia) airplane that is used as the flight demonstrator for the Adaptive Compliant Trailing Edge (ACTE) Project. As a joint effort between NASA, the U.S. Air Force Research Laboratory, and FlexSys Inc. (Ann Arbor, Michigan), the ACTE flight project demonstrates an experimental adaptive

[1]Aerospace Engineer, Aerodynamics and Propulsion Branch / 520, P.O. Box 273, MS 4840B, (661) 276-2645, AIAA Senior Member.

compliant flap in flight.[2] The ACTE flap is a variable-geometry trailing-edge device that is seamless to the surrounding area of the wing of the airplane. The ACTE flap technology has been tested in small-scale flight tests.[3] The NASA AFRC SCRAT expands the flight research of ACTE flap technology to the higher flight loads, Reynolds numbers, and Mach numbers that are representative of typical full-scale jetliners.

Figure 1 shows the ACTE flap installed on the wing of the NASA GIII tail number 804 airplane. The ACTE flaps replace the conventional flaps on both wings. The ACTE flap spans approximately 50 percent of the wing half-span and approximately 20 percent of the wing chord, filling the entire cove of the original GIII flap. Unlike a conventional airplane flap, there are no gaps between the ACTE flap and the rest of the wing, even when the ACTE flap is deflected; the inboard and outboard transition sections provide seamless connections to the surrounding wing surfaces. In addition to replacing the original flaps, the ACTE flap installation required the removal of the ground and flight spoilers from each wing. Some of the GIII wing's vortex generators (VGs) can be seen in the upper left in Fig. 1. For the current flight demonstration effort, the ACTE flap does not move in flight, rather, the deflection of the flap is fixed at a predetermined angle before each flight and remains fixed in that position from takeoff to landing. At 0-deg deflection, the ACTE flap provides a wing outer mold line (OML) that is essentially the same as the clean GIII wing. Positive ACTE flap deflection is defined to be trailing-edge down, as depicted in Fig. 1; negative flap deflection is trailing-edge up from the 0-deg position.

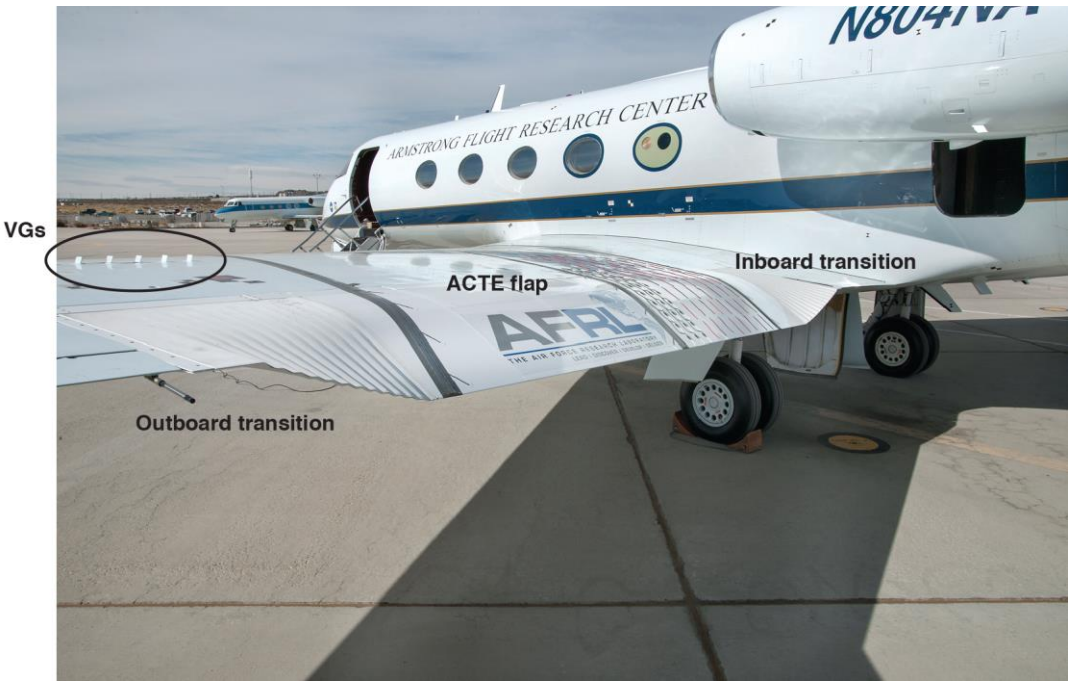

Fig. 1. The Adaptive Compliant Trailing Edge flap on the wing of the NASA Gulfstream III research airplane, tail number 804.

The deflected ACTE flap during the ACTE research flights represents a change in the OML of the GIII wing, so it is important to understand the change produced by the ACTE flap in the GIII wing aerodynamics throughout the entire flight envelope for the ACTE-flap-equipped NASA GIII research airplane. The low-speed stall characteristics of the ACTE wing were analyzed and reported previously.[4] High-speed ACTE wing aerodynamics also need to be analyzed and understood to ensure the airworthiness of the ACTE-equipped airplane over the full range of airplane speeds.

The STAR-CCM+® (Siemens Product Lifecycle Management Software Inc., United States) polyhedral unstructured computational fluid dynamics (CFD) code was used to conduct the high-speed CFD analysis for the ACTE airplane. The CFD methodology is next described. The effects of grid sizes on the accuracy of the CFD predictions then are quantified from a grid convergence study. Finally, CFD solutions for the high-speed aerodynamics of the clean GIII wing as well as the ACTE wing are presented and discussed.

III. Computational Fluid Dynamics Methodology

The Reynolds-averaged Navier-Stokes (RANS) CFD approach was used in this analysis effort. All of the CFD simulations used the flight condition of a Mach number of 0.85 and an altitude of 40,000 ft. Three nominal lift coefficient (C_L) values were considered in this study: 0.2 (low), 0.375 (mid), and 0.5 (high). These are the nominal C_L values for a clean GIII wing with 0-deg flap deflections. Changing the wing configurations - for instance, removing and adding the VGs, deflecting the ACTE flap, turning the engine on or off - changes the pressure distributions over the wing and results in slightly different C_L values. There are therefore two choices: keeping the C_L value constant or keeping the angle of attack (AoA) constant across the various wing configurations. For the present study, the angle of attack (AoA) was kept constant across the different wing configurations, and the wing C_L values were allowed to vary somewhat. The variations in C_L were small compared to the full range of C_L values under consideration and so do not affect the conclusions of this study.

Figure 2 shows the CFD grid. As seen in Fig. 2(a), only one-half of the airplane on a symmetry plane (red in Fig. 2(a)) was analyzed to most efficiently utilize computational resources. At high-speed flows, the flow over the outboard portion of the wing is expected to be complex, therefore, the upper wing surface grid is finer in the outboard section of the wing (green in Fig. 2(a)). Figure 2(b) shows the details of the grid refinements in the vicinity of the GIII wing VGs. There are 31 VGs on the standard GIII wing. They are shown in Fig. 2(b) as straight rows of small blades on the upper surface of the wing just inboard of the winglet. Figure 2(c) shows the detailed surface CFD grid for a VG blade. Manual measurements taken of the NASA GIII airplane indicated that the VGs can be approximated by a simple flat plat with a rounded leading edge and a flat trailing edge. To quantify the effects of the VGs on the aerodynamics of the GIII wing, some CFD simulations were performed without the VGs. The grid refinements shown in Fig. 2 are also present in the CFD simulations without VGs to ensure that the differences in the CFD simulations are caused only by the presence or absence of the VGs and not by any changes in grid topologies. The airplane CAD model was obtained from a laser scan of the GIII NASA tail number 804. The CAD models for the VGs were generated from manual measurements on the SCRAT.

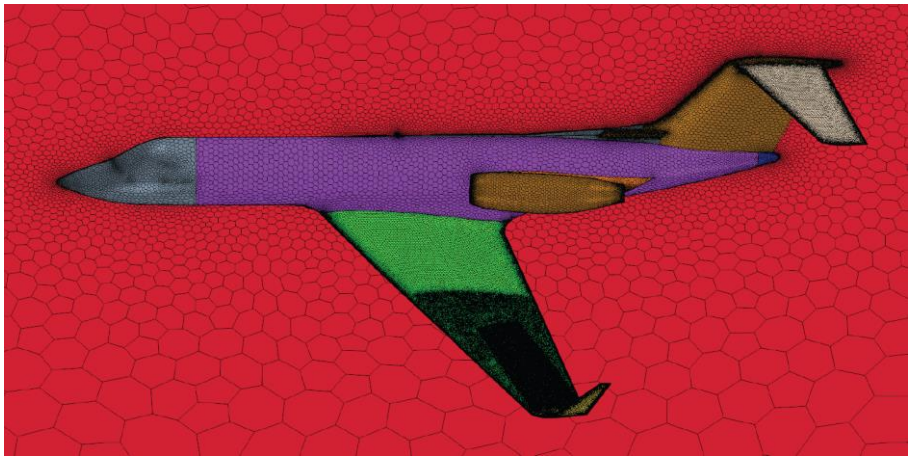

(a) Airplane CFD grid.

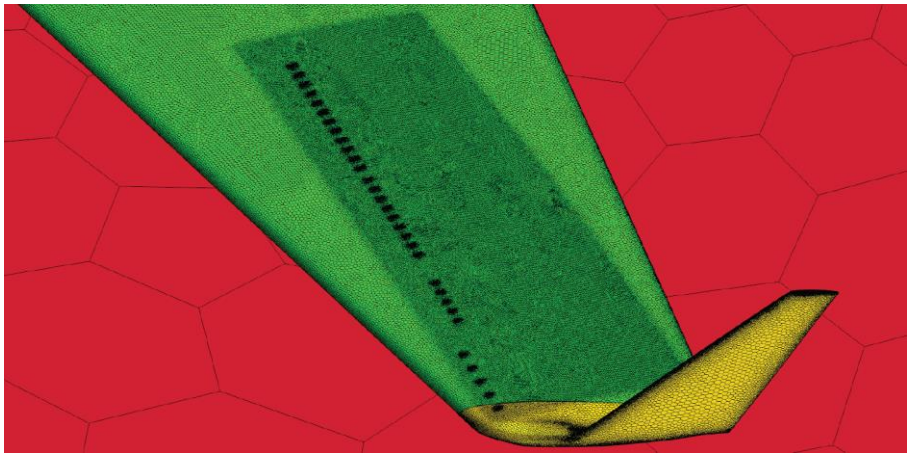

(b) Vortex generator grid refinement details.

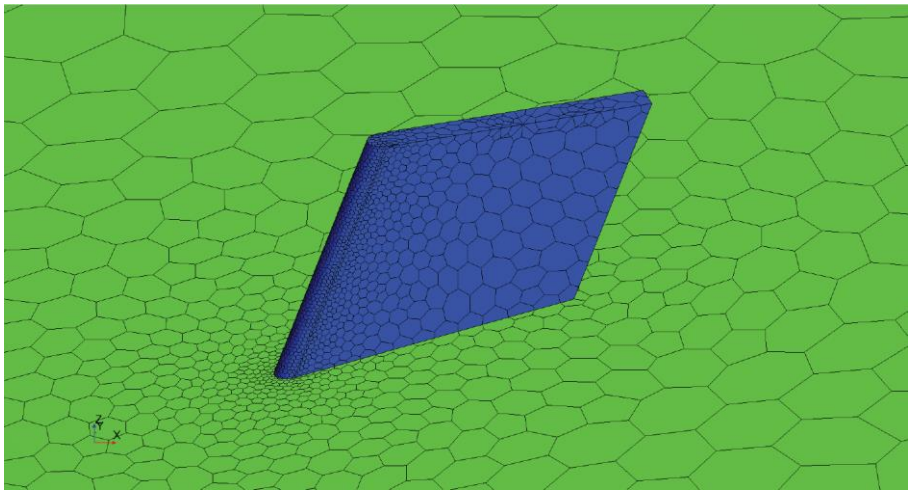

(c) Vortex generator grid details.

Fig. 2. The computational fluid dynamics unstructured polyhedral grid for the NASA Gulfstream III research airplane with vortex generators.

Unstructured polyhedral grids were used together with prism layers to model the near-wall boundary-layer flows. Table 1 presents details of the four different grid sizes that were used for the half-plane grid convergence study: 13.3 (coarse), 20.0 (medium), 30.1 (fine), and 41.9 (finest) million cells. A surface grid growth rate value of 1.3 was used for all grids. To ensure a smooth transition between the surface grid and the volume grid away from the surfaces, a tetrahedral/polyhedral volume growth rate of 1.0 was used. In STAR-CCM+® CFD code terminology, a tetra/poly volume growth rate of 1.0 does not mean that there is no cell volume growth but rather that it is grown at the slowest rate possible in the volume grid.

Table 1. Grid sizes, reference lengths, and number of prism layers.

	Grid size, 10^6 cells	Baseline length, m	Number of prism layers
Coarse	13.3	5.6	19
Medium	20.0	4.4	25
Fine	30.1	3.4	31
Finest	41.9	2.7	31

All of the grid sizes for the surface grid and volume grid were specified as percentages of a single baseline length which was then varied to create the coarse, medium, and fine grids. This gridding strategy was used to ensure that the overall grid topologies stayed similar even as the grids were refined. Table 1 lists the values of the baseline lengths used together with the number of the prism layers for the four different CFD grids. The baseline length of 4.4 m for the 20 million cells grid is close to the mean aerodynamic chord (MAC) of the GIII wing. The MAC is the typical baseline length for the first airplane CFD grid. The nominal CFD grid cell volume being proportional to the length cubed, the original baseline length is divided by $(2)^{1/3}$ in order to obtain the next-finer grid, which should result in cells with half the volumes and be approximately 2 times the number of cells of the original grid. In practice, this procedure only provides approximately a 1.5-times increase in the number of cells from the current grid to the next-finer grid, as can be seen in table 1.

Nineteen prism layers were used for the coarse grid, 25 for the medium grid, and 31 for the fine and finest grids. The prism layers are clustered near wall using the hyperbolic tangent stretching function. Both the total prism layer thickness and the next-to-the-wall prism layer spacing were specified to be constant through the different grid sizes. A total prism layer thickness of 0.03 m was found to provide adequate coverage of the boundary-layer regions over the airplane. The next-to-the-wall prism layer spacing of 2×10^{-5} m in provides an average near-wall y^+ value of approximately 1.0 over the entire airplane ranging from high values of approximately 8 near the leading edge of the winglet to low values of significantly less than 1.0 near the trailing edge of the wing. Generally, near-wall y^+ values are significantly higher on the winglet than on the wing. Near-wall y^+ values are also higher around the wing and winglet leading edges. The SST (Menter's Shear Stress Transport) k-omega two-equation turbulence model was used with automatic wall treatment; turbulence wall function is used automatically in the CFD simulations when the near-wall y^+ value is high enough. Second-order Roe flux difference-splitting was used with a coupled implicit flow solver.

Table 2 lists the common grid parameters used for all grid resolutions. As mentioned previously, the finer grids are obtained simply by reducing the one baseline reference length value while keeping the percentages in table 2 the same across the various grid sizes in order to achieve a family of topologically similar grids.

Table 2. Common CFD grid parameters for all grid resolutions.

Property	Value
Surface curvature	36
Surface mesh growth rate	1.3
Volume mesh growth rate	1.0
Prism layer thickness	0.03 m
First prism layer thickness	2.0×10^{-5} m
Wing minimum surface mesh size	0.35 %
Wing target surface mesh size	3.5 %
Winglet minimum surface mesh size	0.02 %
Winglet target surface mesh size	1.5%
VGs minimum surface mesh size	0.008 %
VGs target surface mesh size	0.08 %
Vertical tail minimum surface mesh size	0.5 %
Vertical tail target surface mesh size	5 %
Horizontal tail minimum surface mesh size	0.25 %
Horizontal tail target surface mesh size	2.5 %
Fuselage minimum surface mesh size	1 %
Fuselage target surface mesh size	8 %
Engine pod minimum surface mesh size	1 %
Engine pod target surface mesh size	6 %

IV. Adaptive Compliant Trailing Edge Airplane High-Speed CFD Results

A. Computational Fluid Dynamics Grid Convergence Study

To ensure that the CFD analysis results obtained in this study do not significantly depend on CFD grid sizes, a CFD grid convergence study was first conducted for the clean baseline GIII wing with 0-deg flap deflection and no VGs. The global forces and moments of the airplane, as well as the local airfoil pressure coefficient (C_p) distribution at a wing station in the middle of the aileron, were evaluated to ensure that global and local flow physics over the wing were sufficiently captured. To avoid the necessity of performing a different grid convergence study for every different C_L value, the worst-case flight condition with the highest C_L value of 0.5 was chosen for this grid convergence study. If a CFD grid is good enough for this worst-case flow, then it should be sufficient for the more benign flows at the lower C_L values. Using the same CFD grid for all of the different C_L values has the added advantage of differences in the solutions are due purely to flow physics and not changes in the CFD grids.

The grid convergence study results are shown in table 3. Percent differences shown in table 3 are referenced to the values for the finest grid of 41.9 million cells. In addition to drag coefficient (C_D), lift coefficient (C_L), and pitching moment coefficient (C_m) results, evaluation was made of the half-airplane side force (C_Y) and rolling moment (C_l) coefficients for indications of grid convergence of the lateral aerodynamic forces and moments on the airplane. As can be seen in table 3, all grid errors consistently decrease as the grids are refined. The largest reduction in grid errors occurs between the medium and fine mesh. All errors between the fine and finest meshes shown in table 3 are less than 4 percent.

Table 3. Grid convergence study results for airplane configuration aerodynamics.

Grid	Grid size, 10^6 cells	C_D	C_D, % diff.	C_L	C_L, % diff.	C_m	C_m, % diff.	C_l	C_l, % diff.	C_Y	C_Y, % diff.
Coarse	13.3	0.05060	5.86	0.5260	3.39	-0.0438	38.31	0.0573	4.91	-0.0700	-0.72
Medium	20.0	0.04903	2.58	0.5177	1.75	-0.0393	24.18	0.0562	2.86	-0.0697	-1.08
Fine	30.1	0.04834	1.12	0.5106	0.35	-0.0328	3.70	0.0549	0.59	-0.0704	-0.04
Finest	41.9	0.04780	0.00	0.5088	0.00	-0.0317	0.00	0.0546	0.00	-0.0705	0.00

Figure 3 shows the grid refinement results for the local airfoil C_p distribution at a spanwise wing station in the middle of the aileron (wing buttline station BL 354). This wing station was chosen based on previous airworthiness CFD analysis work on the SCRAT[5] that found complex shock and boundary-layer interactions near this location for high-speed flight conditions. All of the subsequent airfoil sectional Cp plots and Mach number contour plots in this report were obtained for this spanwise wing station at BL 354.

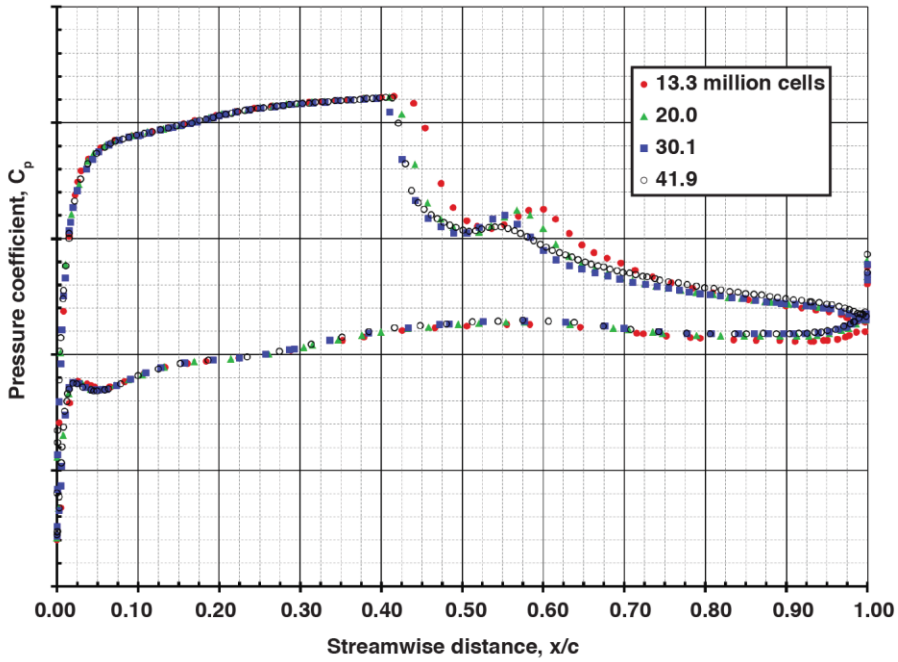

Fig. 3. Grid convergence results for airfoil Cp distribution at the spanwise wing station BL 354 in the middle of the aileron.

In Fig. 3 more negative C_p values are plotted toward the top of the vertical axis. It can be seen from Fig. 3 that all grid sizes give results that generally agree for the C_p distribution along both the upper and lower surfaces of the airfoil. Discrepancies between the various grids are found mostly on the upper wing surface at streamwise-distance/airfoil-chord (x/c) locations between 0.4 and 0.7. The coarse grid predicts the shock to be noticeably downstream of the finer grids. Also, there are differences in the C_p results after the shock at approximately x/c = 0.6 for various grid sizes.

It can be seen that for all grid sizes the CFD solutions consistently converge to the finest grid results for the global forces and moments of the airplane, as well as for the local airfoil C_p distributions. To minimize grid-related errors, the finest grid of 41.9 million cells was used for all subsequent studies in the current effort.

B. Airplane Lift Effects on Wing Flow Quality

Figure 4 compares the local airfoil C_p distribution for three different nominal C_L values: low (0.2), mid (0.375), and high (0.5) for the clean baseline GIII wing with 0-deg flap deflection and no VGs. It can be seen that the higher C_L values move the shock location farther upstream on the upper surface of the wing. Also, the C_p value at the airfoil trailing edge becomes more negative for higher C_L values. Generally, higher C_L values are expected to result in more complex flows over the wing. Indications of a more complex flow over the wing, therefore, based on the results shown in Fig. 4, include a more upstream shock and a more negative trailing-edge C_p value.

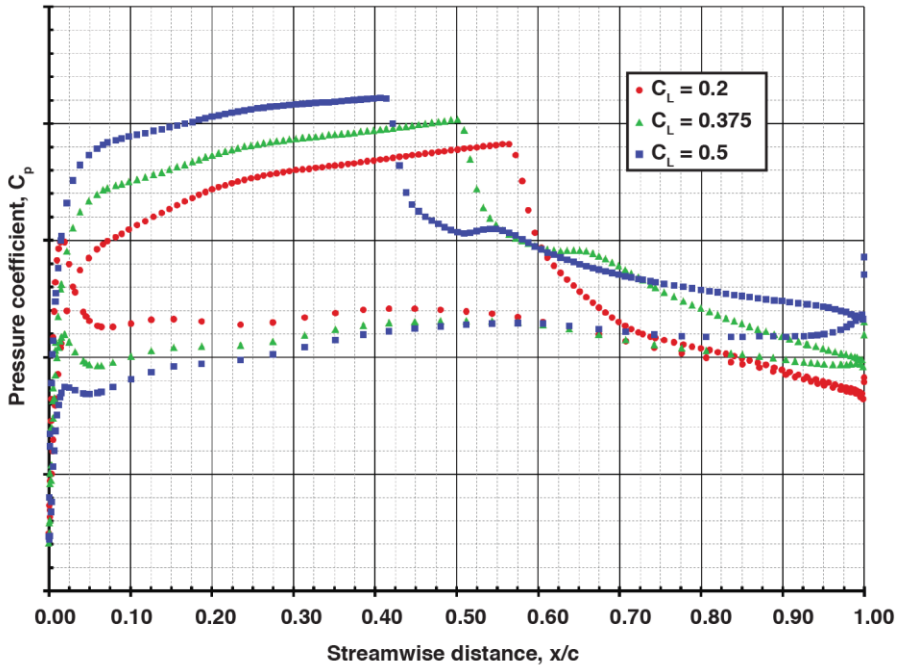

Fig. 4. Lift effects on the wing airfoil C_p distribution at the spanwise wing station in the middle of the aileron.

Figure 5 shows the Mach number contours. The red outline on the upper surface of the airfoil near the trailing edge in these Mach contour plots indicates the presence of a flow separation bubble. Figure 5(a) shows that at the low-C_L value the shock on the upper surface of the airfoil is relatively weak, and the resulting minimal flow separation bubble does not significantly change the effective outer mold line of the airfoil section resulting in a relatively smooth and benign flow field over the airfoil as expected.

Figure 5(b) shows that the shock becomes stronger at the mid-C_L value, and a larger flow separation bubble is predicted. The interruption to the flow field over the rest of the airfoil, however, is still small. In contrast, Fig. 5(c) shows that at the high-C_L value of 0.5 the shock becomes very strong, causing extensive flow separation over the top wing surface covering more than half of the chord of the airfoil. Since this spanwise wing station is located in the middle of the aileron, it is likely that the airplane would experience wing buffet as well as unsatisfactory lateral control characteristics near this high-C_L value.

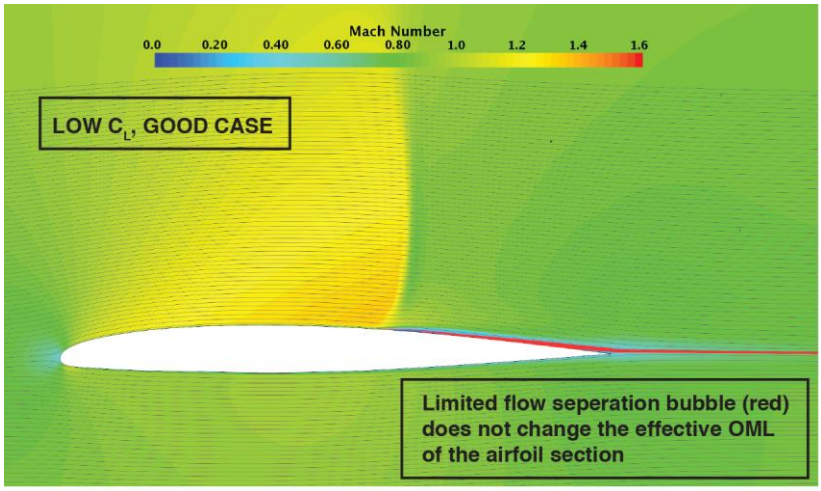

(a) C_L = 0.2.

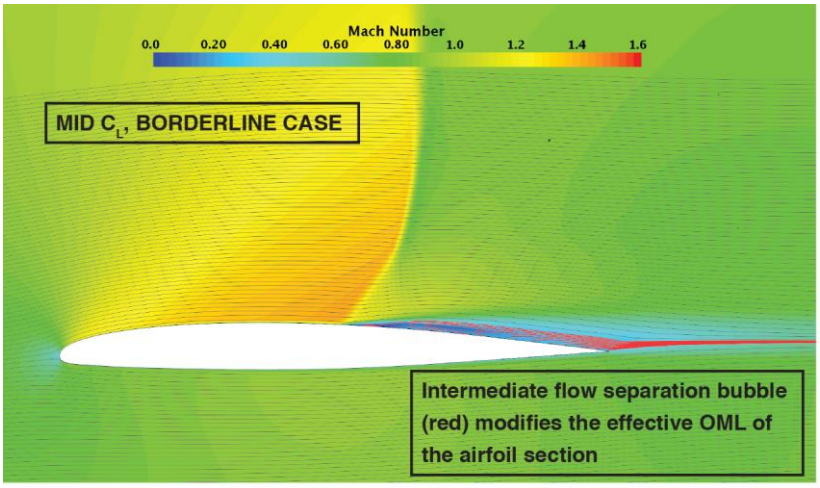

(b) C_L = 0.375.

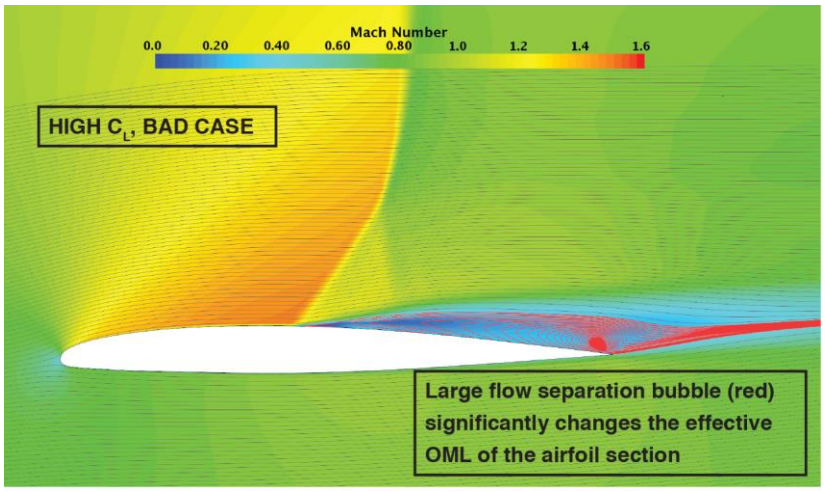

(c) C_L = 0.5.

Fig. 5. Lift effects on the Mach number contours at the spanwise wing station in the middle of the aileron.

In summary, the CFD results of the present study find benign wing aerodynamics for the low-C_L value of 0.2, somewhat worse but still acceptable wing aerodynamics for the mid-C_L value of 0.375, and unacceptable wing aerodynamics for the high-C_L value of 0.5 with extensive flow separation at the location of the aileron and high potential for wing buffet and unsatisfactory lateral control characteristics.

C. Airplane Engine Effects

When controllability problems are encountered in an airplane at high speeds, a typical mitigation is to cut back the engine throttles to reduce airspeed; however, it was observed from previous in-house CFD analyses on the SCRAT that the flows induced by the operating engine inlets affect wing aerodynamics, and it was unclear whether cutting back the engine throttle would improve or worsen wing aerodynamics. Therefore, an engine-off CFD simulation was performed for the mid-C_L value. Instead of performing several CFD simulations for various intermediate engine throttle settings, we chose the engine-off case with no flow at all for the completely blocked engine to study the worst-case effects of cutting back the engine throttles.

Figure 6 compares the C_p distributions between the mid-C_L engine-off result with the various engine-on results at different C_L values. It can be seen that turning the engine off has a net positive effect on the wing aerodynamics at this spanwise location. The shock in the upper surface of the wing of this mid-C_L case is positioned even further downstream than the engine-on low-C_L shock. Although the mid-C_L value was used, the C_p value at the airfoil trailing edge is approximately the same as the engine-on low-C_L shock, indicating more benign flows.

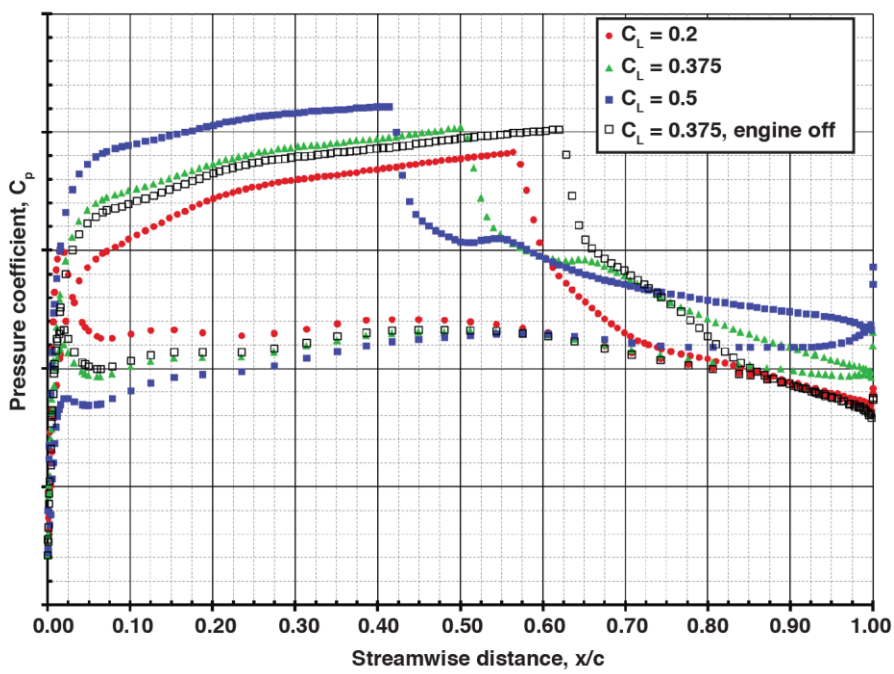

Fig. 6. Airplane engine effects on the wing airfoil C_p distribution at the spanwise wing station in the middle of the aileron.

The Mach number contours shown in Fig. 7 reinforce the conclusion that cutting back the engine throttles improves wing aerodynamics. At the mid-C_L value, it can be seen that the flow separation bubble has shrunk and is comparable in size to the engine-on low-C_L case shown in Fig. 5(a), and is therefore much smaller than the engine-on mid- and high-C_L cases shown in Figs. 5(b) and 5(c), respectively.

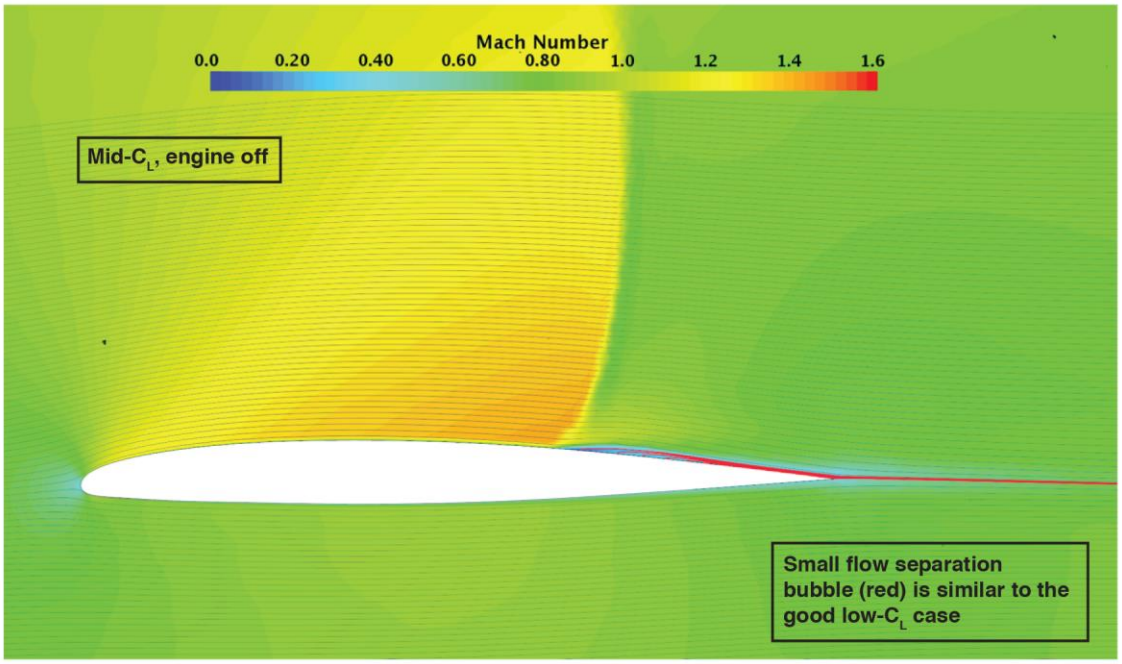

Fig. 7. Airplane engine effects on the Mach number contours at the spanwise wing station in the middle of the aileron.

In summary, our current CFD results indicate that the high-speed wing aerodynamics of the GIII airplane actually improve with the engines throttled back or turned off altogether. Therefore, when the GIII encounters unexpected problems during high-speed flights, the airplane can be slowed down safely by cutting back the engine throttles.

D. Wing Vortex Generators Effects

As shown in Fig. 2(b), 31 wing VGs are installed on each of the GIII wings. Our in-house CFD analysis work found that although the VGs have minor influences on wing aerodynamics at low-speed flight, the VGs have significant effects on wing aerodynamics at high-speed flight. Figure 8 shows the Mach number contours at BL 354. The ripples in the Mach contours upstream of the shock did not appear in the CFD results without VGs and were likely caused by the additional flow mixing introduced by the VGs. When compared to the no-VGs mid-C_L results in Fig. 5(b) it can be seen that the flow separation bubble on the top of the airfoil has been completely eliminated here for the case with the VGs. The flow improvement with VGs on is even better than what was observed with the engine-off case shown in Fig. 7, where a small flow separation bubble can still be seen near the trailing edge.

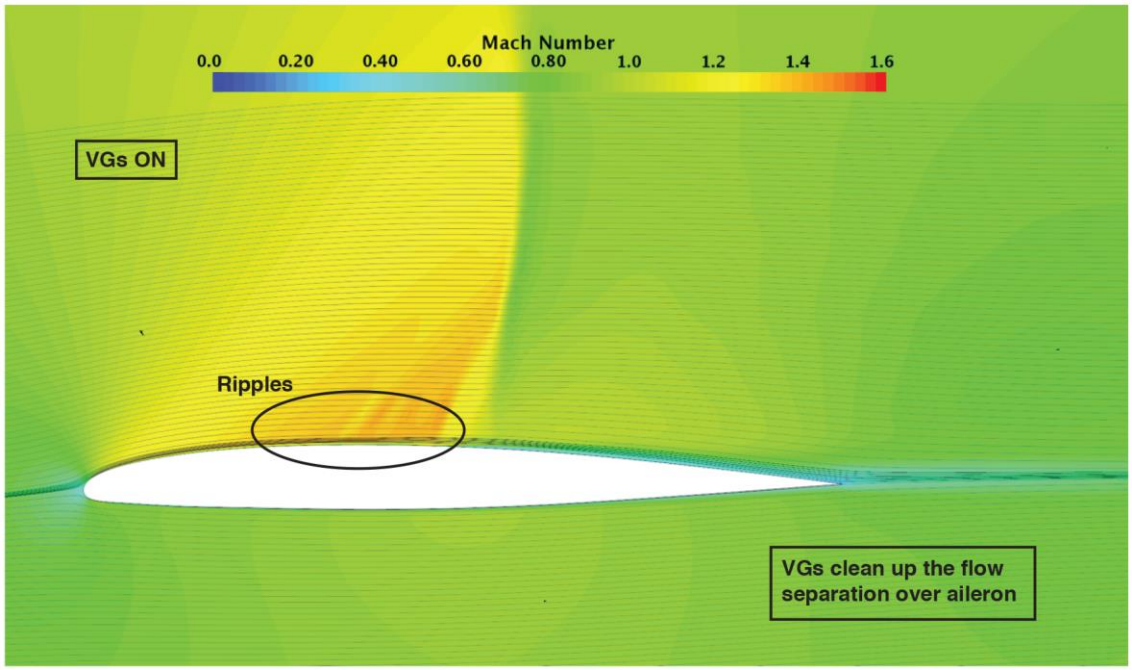

Fig. 8. Wing vortex generators effects on GIII wing aerodynamics, mid-C_L value.

In summary, the VGs are found to eliminate the flow separation bubble for the mid-C_L case. This condition would improve wing aerodynamics as well as aileron effectiveness, allowing normal operation of the airplane at a Mach number of 0.85.

E. Adaptive Compliant Trailing Edge Flap Deflection Effects

To investigate the ACTE flap deflection effects on the GIII wing at high speeds, CFD simulations were performed for ACTE flap deflections of 1- and 2-deg trailing-edge-down with wing VGs modeled at the mid-C_L value. The ripples in the Mach contours caused by the additional mixing by the VGs can be seen in Figs. 9(a) and 9(b).

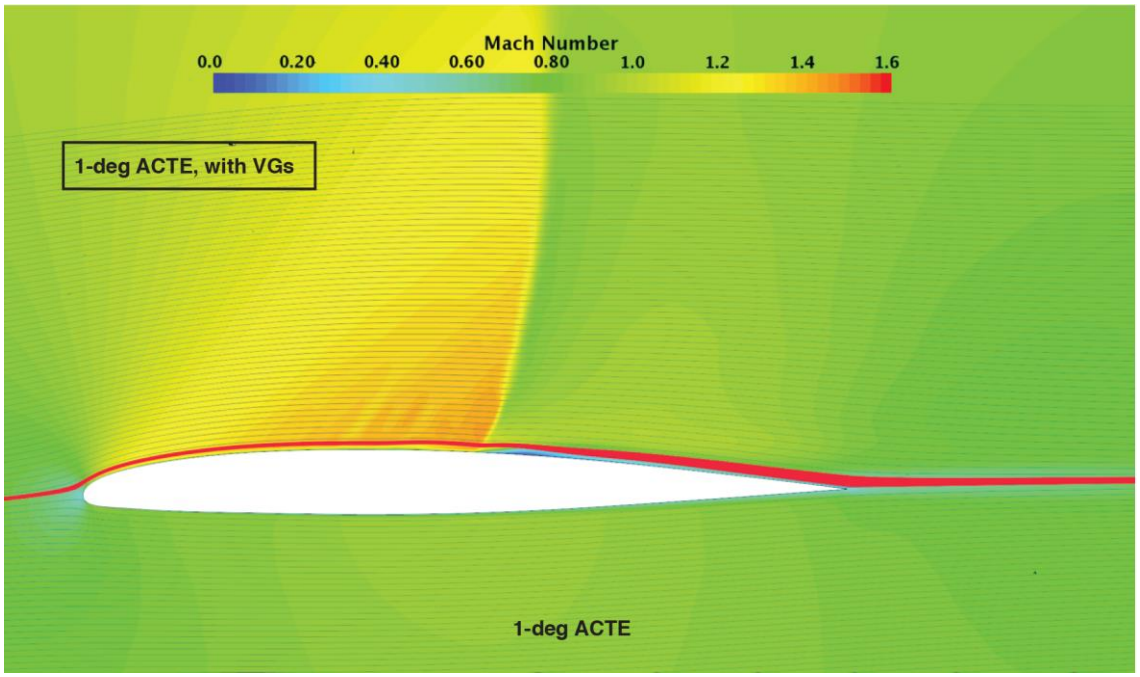

(a) 1-deg ACTE flap deflection.

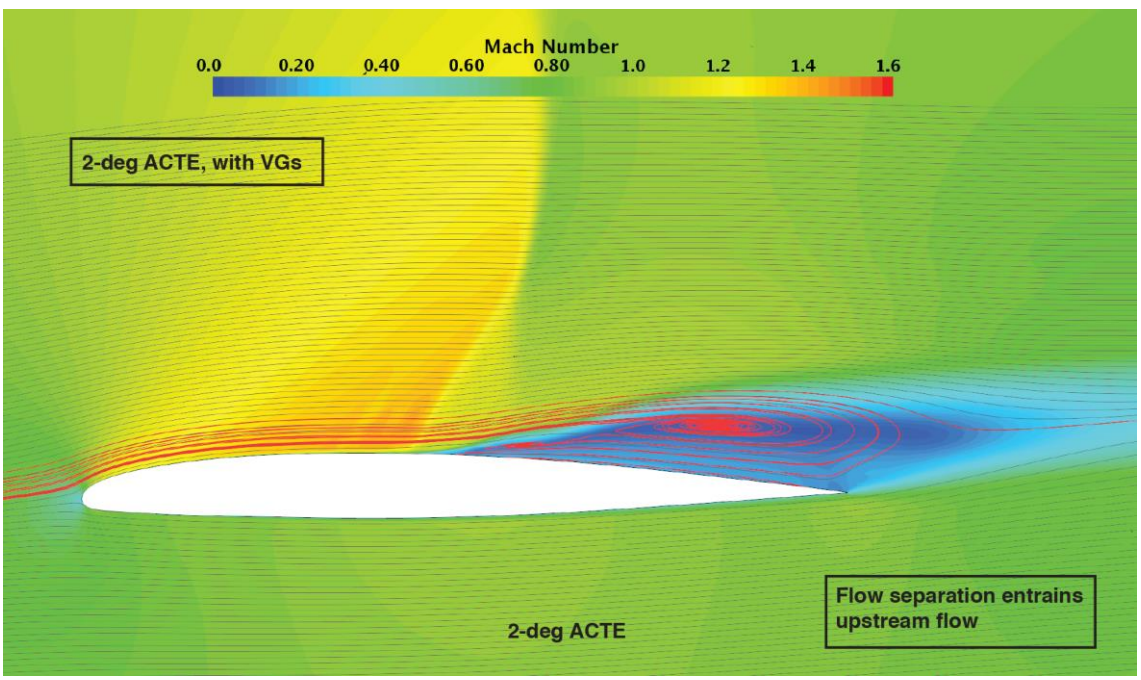

(b) 2-deg ACTE flap deflection.

Fig. 9. Adaptive Compliant Trailing Edge flap deflection of 2-deg effects on GIII wing aerodynamics, mid-C_L value.

The results in Figs. 9(a) and 9(b) clearly show that the ACTE flap deflections negate the aerodynamic benefits provided by the wing VGs. Whereas the VGs on the clean baseline GIII wing eliminate the flow separation bubble altogether (Fig. 8), Fig. 9(a) shows that an ACTE flap deflection as small as 1 deg brings back a small flow separation bubble and the potential flow unsteadiness associated with shock-induced flow separation. Deflecting the ACTE flap to 2 deg causes the largest and most extensive flow separation region seen in this study, as shown in Fig. 9(b). Here,

even with the VGs present, the flow separation region is even larger than that of the high-C_L-no-VGs result shown in Fig. 5(c). In addition, instead of a local recirculating flow separation bubble as found in Fig. 5(c), Fig. 9(b) shows that the flow separation region for the 2-deg ACTE flap extends further into the core flow and entrains more core flows into this separated flow region, making likely a larger disturbance to the flow and giving rise to potentially even more serious wing aerodynamics and controllability problems than even the high-C_L-no-VGs result shown in Fig. 5(c).

Figure 10 provides the CFD visualizations for the wing surface C_p color contours with the flow surface streaklines superimposed for the nominal mid-C_L value of 0.375. The clean baseline GIII wing with no VGs and 0-deg flap deflection is shown in Fig. 10(a). It can be seen that the two inboard shocks over the wing merge and form a single shock outboard of the wing in front of the aileron. When the VGs are modeled in front of the aileron as shown in Fig. 10(b), it can be seen that the additional flow mixing by the VGs causes the shock line in front of the aileron to be jagged/V-shaped and no longer the straight line seen in Fig. 10(a). Also, prominent flow vortices are formed downstream of the VGs. When the ACTE flap is deflected 2 deg trailing-edge-down as shown in Fig. 10(c), it can be seen that a new inboard flow separation occurs over the ACTE flap near the trailing edge of the wing. The mixing action of the VGs seen in Fig. 10(c) appears to be less vigorous, with fewer V-shapes in the shock line and fewer flow vortices downstream of the VGs. It is interesting to note that two different effects are observed here: the local mixing effects of the outboard VGs, and the non-local effects of the deflected inboard ACTE flap. Both influence the outboard wing aerodynamics in front of the aileron.

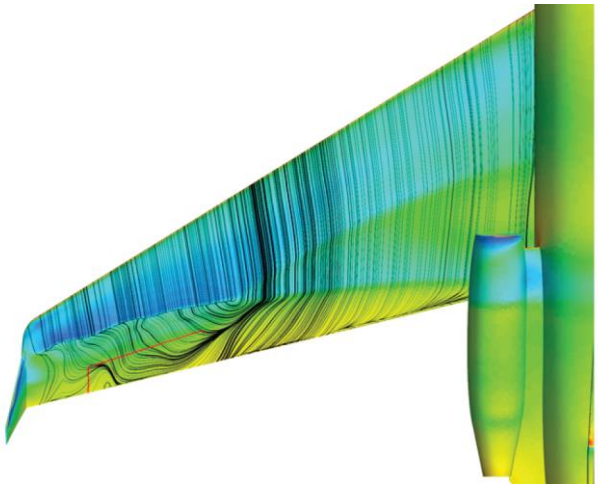

(a) Clean baseline GIII wing with no VGs and 0-deg flap deflection.

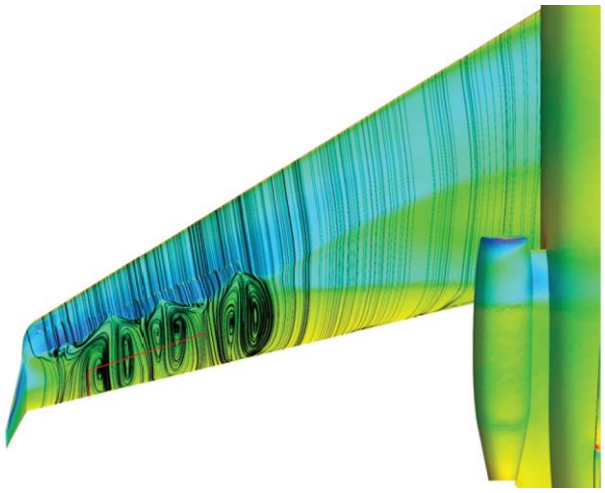

(b) Clean baseline GIII wing with VGs.

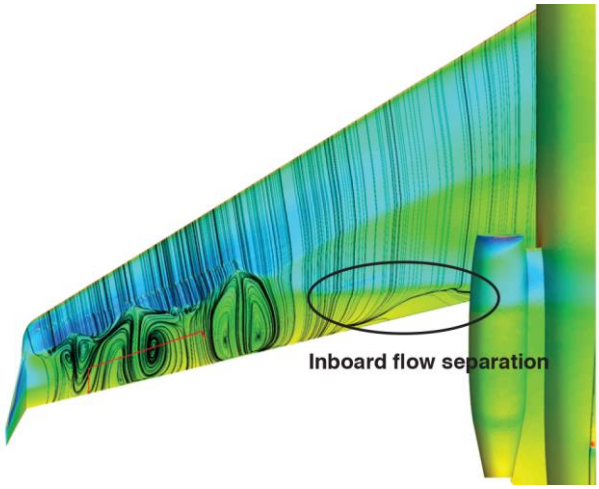

(a) ACTE GIII wing with VGs and 2-deg flap deflection.

Fig. 10. Adaptive Compliant Trailing Edge wing pressure coefficient contours with flow streaklines, mid-C_L value: C_L = 0.375.

In summary, at the mid-C_L value the ACTE flap deflections were found to completely remove the aerodynamic benefits of the VGs for the 1-deg ACTE flap. For the 2-deg ACTE flap, the flow separation over the airfoil for the mid-C_L value was found to be extensive and worse than the baseline clean GIII wing without VGs at high C_L. Both the 1-deg and 2-deg ACTE flap deflections would likely result in wing aerodynamics and controllability problems in high-speed flight. Flow visualizations show that trailing-edge devices such as the ACTE flap can affect the aerodynamics in other locations of an actual airplane wing. For example, the current ACTE flaps are located inboard at the trailing edge of the wing but they adversely affect the air flows in the outboard stations of the wing in front of the aileron. Future designs and applications of wing trailing-edge devices should not limit design analysis work to two-dimensional airfoils but also consider possible effects on the entire extent of a three-dimensional wing. Also, analyses should be conducted for the entire expected speed range.

As the results of the current analysis, the flight project decided to fly the ACTE airplane with only 0-deg ACTE flap deflection at high speeds.

V. Conclusion

Computational fluid dynamics (CFD) analysis was conducted to evaluate the high-speed aerodynamics of a Gulfstream GIII airplane (Gulfstream Aerospace Corporation, Savannah, Georgia) swept wing modified with an experimental seamless, compliant flap called the Adaptive Compliant Trailing Edge (ACTE) flap for airworthiness. The high-speed aerodynamics of the modified ACTE wing were analyzed at the flight condition of a Mach number of 0.85 and an altitude of 40,000 ft using a polyhedral finite-volume unstructured Reynolds-averaged Navier-Stokes CFD code. Three different lift coefficients (C_L) were considered: low, mid, and high. Wing aerodynamics sensitivities to C_L, engine operation, vortex generators (VGs), and ACTE flap deflections were examined. High-speed flows over the unmodified GIII wing were found to be highly complex with three-dimensional shock and boundary-layer interactions over the upper wing surface. Without the VGs, the GIII wing was found to have shock-induced flow separations near the aileron at all C_L values, which could cause buffet and controllability problems at the mid- and high-C_L values under consideration. The CFD solutions showed that the VGs improve the high-speed aerodynamics of the baseline clean GIII wing at the mid-C_L value, as expected; however, ACTE flap deflections of as little as 1 to 2 deg negated all of the aerodynamic improvements from the VGs. In addition, this inboard trailing-edge modification device was found to adversely affect the aerodynamics of the flow at a different location on the wing away from the ACTE flap itself - in the outboard region of the wing in front of the aileron. This CFD analysis was important to the flight planning for the current phase of high-speed ACTE flight demonstration. The project dropped the high-speed flights for all planned ACTE flap deflections and only flew the 0-deg ACTE flap. The current CFD analysis has identified potentially serious aircraft controllability problems before flying and made an important contribution to the airworthiness and flight safety review process at the NASA Armstrong Flight Research Center for our high-speed ACTE flight demonstration project.

References

[1] Baumann, E., Hernandez, J., and Ruhf, J., "An Overview of NASA's SubsoniC Research Aircraft Testbed (SCRAT)," AIAA-2013-5083, 2013.
doi: 10.2514/6.2013-5083

[2] Cumming, S., Smith, M. S., Ali, A. N., Bui, T. T., Ellsworth, J. C., and Garcia, C. A., "Aerodynamic Flight Test Results for the Adaptive Compliant Trailing Edge," AIAA-2016-3855, 2016.
doi: 10.2514/6.2016-3855

[3] Kota, S., Osborn, R., Ervin, G., Maric, D., Flick, P., and Paul, D., "Mission Adaptive Compliant Wing – Design, Fabrication, and Flight Test," RTO-MP-AVT-168, pp.18-1–18-19, 2009.

[4] Bui, T. T., "Analysis of Low-Speed Stall Aerodynamics of a Swept Wing with Seamless Flaps," AIAA-2016-3720, 2016.
doi: 10.2514/6.2016-3720

[5] Smith, M. S., Bui, T. T., Garcia, C. A., and Cumming, S. B., "Longitudinal Aerodynamic Modeling of the Adaptive Compliant Trailing Edge Flaps on a GIII Aircraft and Comparisons to Flight Data," AIAA-2016-3703, 2016.
doi: 10.2514/6.2016-3703